REVIEW

National Science Review
3: 520–533, 2016
doi: 10.1093/nsr/nww062
Advance access publication 26 September 2016

CHEMISTRY

Rational design and synthesis of noble-metal nanoframes for catalytic and photonic applications

Xue Wang[1,2], Aleksey Ruditskiy[3] and Younan Xia[1,3,*]

ABSTRACT

Nanoframes are unique for their 3D, highly open architecture. When made of noble metals, they are attractive for use as heterogeneous catalysts because of their large specific surface areas, high densities of catalytically active sites and low vulnerability toward sintering. They promise to enhance the catalytic activity and durability while reducing the material loading and cost. For nanoframes composed of Au and/or Ag, they also exhibit highly tunable plasmonic properties similar to those of nanorods. This article presents a brief account of recent progress in the design, synthesis and utilization of noble-metal nanoframes. We start with a discussion of the synthetic strategies, including those involving site-selected deposition and etching, as well as dealloying of both hollow and solid nanocrystals. We then highlight some of the applications enabled by noble-metal nanoframes. Finally, we discuss the challenges and trends with regard to future development.

Keywords: noble metal, nanoframe, nanomaterial synthesis, catalysis, plasmonics

[1]The Wallace H. Coulter Department of Biomedical Engineering, Georgia Institute of Technology and Emory University, Atlanta, GA 30332, USA; [2]State Key Laboratory for Oxo Synthesis and Selective Oxidation, Suzhou Research Institute, Lanzhou Institute of Chemical Physics, Chinese Academy of Sciences, Lanzhou 730000, China and [3]School of Chemistry and Biochemistry, Georgia Institute of Technology, Atlanta, GA 30332, USA

*Corresponding author. E-mail: younan.xia@bme.gatech.edu

Received 12 July 2016; **Revised** 3 September 2016; **Accepted** 5 September 2016

INTRODUCTION

Noble-metal nanocrystals have been extensively explored for many decades due to their use in a plethora of applications related to catalysis, electronics, photonics, information storage, energy conversion and biomedicine [1–6]. Due to the extremely low abundance of these metals in the Earth's crust and their consequently high prices, there is a pressing need to develop the most efficient use of these metals, particularly in catalysis. In recent years, a number of strategies have been demonstrated for increasing the catalytic activity of noble-metal nanocrystals and thereby reducing their loading in a catalyst [7–15]. In addition, the utilization efficiency of a noble metal can be greatly increased by switching to nanostructures with hollow interiors [16–19] or structures in the form of ultrathin nanosheets [20–22].

Many different types of hollow nanostructures have been reported, including the nanoshell, nanobox, nanocage and nanoframe [18,19,23–29]. While all these structures share a unique feature of a hollow interior, they differ substantially in terms of wall porosity. Specifically, both nanoshell and nanobox possess solid walls with no openings, whereas nanocage may contain multiple holes scattered in its walls. Nanoframe is a logical extension of this trend and is characterized by the complete removal of walls. In a sense, a nanoframe is only composed of corners and edges that would normally outline a 3D solid nanocrystal of the same morphology. The result is a framework with a highly open, 3D architecture, particularly when compared with other similarly sized hollow nanostructures. This configuration is of great interest for heterogeneous catalysis as the open structure of a nanoframe allows the molecules involved in a catalytic reaction to readily access atoms in the inner surface of a catalytic particle, thereby increasing the utilization efficiency of the noble metal. The catalytic activity can be further improved by the large specific surface area of a nanoframe, together with the presence of highly active sites such as low-coordinated atoms, steps and kinks [7,30,31]. When compared with the nanoparticles currently used in commercial catalysts, nanoframes also possess greater morphological and compositional stabilities, allowing them to withstand the harsh physiochemical environment of a chemical reactor [26]. Generally, the large specific surface area of a conventional catalyst is

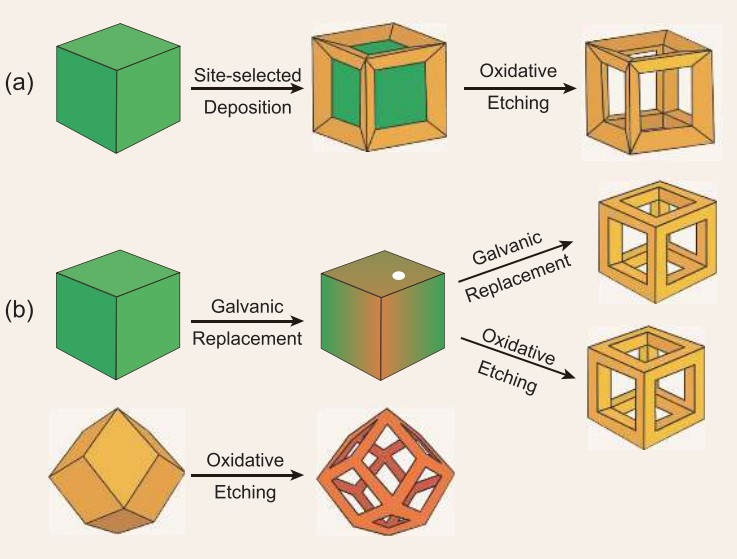

Figure 1. Schematics showing the two strategies that have been reported for the synthesis of nanoframes: (a) site-selected deposition and etching and (b) dealloying.

achieved by decreasing the nanoparticles' size. In the course of long-term reactor operation, the small catalytic particles tend to aggregate or sinter, resulting in substantial decrease for the catalytic activity [32]. In contrast, the unique architecture of nanoframes can retain the large specific surface area while effectively mitigating both aggregation and sintering. The increase in contact area and thus interaction with a catalytic support also make nanoframes less susceptible toward surface migration.

In addition to their superior performance as heterogeneous catalysts, nanoframes have been shown to possess unique optical properties such as localized surface plasmon resonance (LSPR), which arise from the collective oscillation of free electrons in resonance with the incident light [33–41]. During this process, the incident light can be effectively absorbed and then converted to photons (i.e., scattering) or phonons (i.e., absorption or heating). The ratio of photon absorption to scattering, as well as the wavelength of light at which LSPR occurs, is found to be dependent on both the size and shape of the nanostructure, as well as the dielectric environment [42,43]. For nanostructures with nonunity aspect ratios, such as nanorods, there exist two distinct LSPR modes corresponding to the longitudinal and transverse dimensions [44]. When examining their optical properties, nanoframes can be considered as an assembly of multiple nanorods. As such, nanoframes composed of Au and/or Ag display unique LSPR properties that can be readily tuned by changing the edge length relative to the ridge thickness of the nanoframes [33,34].

In this review, we begin with a brief account of the major synthetic methods that have been developed for the preparation of noble-metal nanoframes. As illustrated in Fig. 1, these synthetic protocols are built upon two strategies: (i) site-selected deposition and etching and (ii) dealloying of hollow and solid bimetallic (or multi-metallic) nanocrystals. The hollowing-out mechanisms underlying these strategies can be attributed to galvanic replacement, oxidative etching, intra-particle atomic diffusion or a combination of them. We then highlight some of the applications of nanoframes in the context of photonics and catalysis. Finally, we conclude this review with a discussion of the current challenges and future developments for this new class of nanomaterials.

RATIONAL DESIGN AND SYNTHESIS

The synthetic strategies currently available for the creation of noble-metal nanoframes can be separated into two major categories: (i) the deposition of metal onto specific sites of a template nanocrystal, followed by selective removal of the said template by etching, and (ii) the reshaping of an existing nanocrystal into a nanoframe through the systematic extraction of atoms from the target structure by employing dealloying or etching processes. Depending on the noble metals involved, one can choose to pursue the synthesis using either of these two approaches. From the perspective of rational design, one can manipulate the experimental conditions to maneuver the elemental composition, surface structure, overall morphology and physical dimensions of the nanoframes to optimize their performance for the application of interest.

Site-selected deposition and etching

This is a simple and straightforward strategy for fabrication of noble-metal nanoframes. It involves selective deposition of one metal onto certain regions of a nanocrystal (i.e., the seed or template) composed of another metal (typically, more reactive than the metal to be deposited), followed by selective removal of the seed via chemical etching (Fig. 1a). Experimentally, site-selected deposition can be accomplished through different strategies, including utilizing the difference in free energy between different sites on the surface of a nanocrystal, physically blocking atomic deposition and imposing a kinetic control over the deposition process by modulating the relative rates for atom deposition and diffusion. In general, the rate of atom diffusion is governed by the diffusion constant, $\mathcal{D}$, which can be

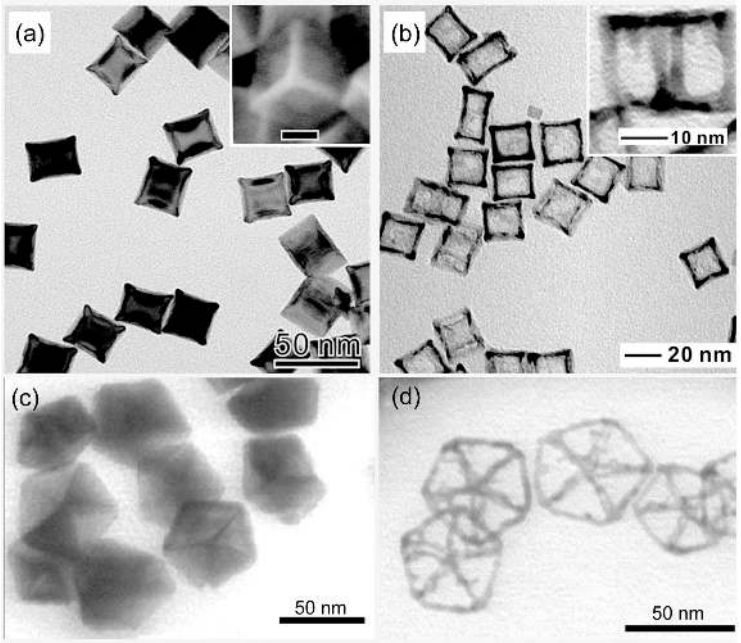

Figure 2. (a) TEM and SEM (inset) images of Pd-Rh core-frame nanocubes. The scale bar in the inset is 10 nm. (b) TEM images of Rh cubic nanoframes obtained by selectively etching away the Pd cores from the core-frame nanocubes. (c) TEM image of Ag decahedra after Au deposition at the edges. (d) TEM image of Au decahedral nanoframes after the dissolution of Ag with H_2O_2. The amount of Au deposited relative to Ag in the template was 7 mol%. Adapted with permissions from [46,53].

expressed by the following equation:

$$\mathcal{D} = \mathcal{D}_0 \exp\left(-\frac{E_{\text{diff}}}{RT}\right), \qquad (1)$$

where $\mathcal{D}_0$ is the diffusion pre-exponential factor, E_{diff} is the potential energy barrier to diffusion, R is the ideal gas constant, and T is the absolute temperature [45]. Thus, atom diffusion increases with increasing T and decreases with increasing E_{diff}. Both parameters can be controlled by varying the experimental conditions.

In one of the early examples, it was demonstrated that Rh atoms could be selectively deposited onto the vertices and edges of Pd nanocubes whose side faces were passivated by a chemisorbed capping agent such as Br^- ions. This led to the formation of Pd-Rh nanocubes with a core-frame structure and concave side faces (Fig. 2a) [46]. The site-selected deposition can be attributed to the preferential chemisorption of Br^- ions on the Pd{100} side faces [47], together with the kinetic control enabled by the dropwise addition of the Na_3RhCl_6 precursor. The Br^- ions could physically prevent the Rh from being deposited on the Pd{100} facets, forcing the Rh atoms to nucleate and grow from the corners and edges. The relatively slow injection rate for the Na_3RhCl_6 precursor saved the newly formed Rh atoms from homogeneous nucleation in the reaction solution and helped achieve a kinetic control over the growth process. The Pd-Rh core-frame nanocubes were subsequently subjected to chemical etching with a combination of Fe^{3+} and Br^- ions. When optimized, the Pd in the cores could be selectively oxidized and dissolved, leaving behind Rh nanoframes with a ridge thickness as thin as 3 nm (Fig. 2b).

The etching of a metal involves a redox reaction and thereby requires a sufficient difference in reduction potential between the etchant and the metal in order to occur, with a larger difference corresponding to a higher rate of etching. The introduction of Br^- was critical to the selective removal of Pd cores by etching. Since the difference in standard reduction potential between the Fe^{3+}/Fe^{2+} (0.77 V *vs.* standard hydrogen electrode or SHE) and $PdCl_4^{2-}/Pd^0$ (0.59 V *vs.* SHE) pairs is too small to provide a sufficient driving force for the etching of Pd, the addition of Br^- was able to increase the driving force for the oxidative etching by forming $PdBr_4^{2-}$ (0.49 V *vs.* SHE for $PdBr_4^{2-}/Pd^0$) [48]. It should also be noted that elevation of temperature, as well as the increase in concentration of the etchant, would lead to accelerated etching rates. The overall reaction can be summarized as follows:

$$Pd + 2Fe^{3+} + 4Br^- \xrightarrow{\Delta} PdBr_4^{2-} + 2Fe^{2+}. \qquad (2)$$

When nano-sized Pd cuboctahedra and octahedra were used as the templates, Rh nanoframes with cuboctahedral and octahedral shapes could also be obtained through site-selected deposition of Rh, followed by selective removal of the Pd cores [49]. Through this strategy, we have also recently prepared Pt cubic nanoframes by employing Pd nanocubes as the templates [50]. Yang and co-workers reported a similar approach to the production of Pd-Rh bimetallic nanoframes by employing a one-pot synthesis to prepare the core-frame nanostructures, followed by etching with nitric acid [51].

Recently, the scope of this approach was further extended by Xia and co-workers to synthesize Ru nanoframes with ridges as thin as 2 nm [52]. In a typical synthesis, Ru was selectively deposited on the vertices and edges of Pd octahedral templates with truncated corners by introducing the $RuCl_3$ precursor at a very slow rate, thus forming Pd-Ru core-frame octahedra. The selected deposition at the {100} corners and {110} edges of an octahedron was achieved by utilizing a combination of the difference in surface free energies and kinetic control. Specifically, the initial deposition of Ru atoms occurred at these sites primarily due to the lower coordination numbers of their constituent atoms,

corresponding to higher surface free energies relative to the {111} side faces. For a face-centered cubic (*fcc*) metal, the free energy hierarchy follows the order of {110} > {100} > {111} in the absence of any capping agent. Since no surface blocking species was present, the initial deposition of the Ru was largely guided by the relative surface energies. Following their deposition, the Ru adatoms could diffuse across the surface of a Pd template. Typically, if the rate of diffusion greatly exceeds the rate of atom deposition, a smooth conformational shell will be formed around the template. Conversely, if this relationship is reversed, the newly deposited atoms will pile up at their initial deposition sites, thereby creating a core-frame structure. By lowering the reaction temperature, it was possible to suppress atom diffusion and thus achieve kinetically enabled buildup at the corners and edges of a Pd template. Again, the Pd cores could be selectively removed using an etchant based upon the Fe^{3+}/Br^{-} pair, leaving behind Ru octahedral nanoframes.

Kitaev and co-workers reported the synthesis of Au nanoframes with ultrathin ridges via edge-selected deposition on Ag decahedral templates [53]. In this case, Au was selectively deposited along the edges of a Ag decahedron under optimized reduction conditions. This was facilitated by tuning the concentration of the reducing agent, the pH of the reaction solution, as well as the amount and injection rate of the $HAuCl_4$ precursor. When the deposition of Au was performed at pH of 8–9, with ascorbic acid (AA) serving as a reducing agent, the decahedral morphology of the original template could be retained up to the deposition of ~15% Au (molar percentage in the nanostructure) due to the formation of a conformal shell (Fig. 2c). When the pH was increased, the reduction power of AA would be enhanced, resulting in higher deposition rates for the Au atoms and thus buildup at the edge sites of a decahedral template. Upon etching of the Ag cores with H_2O_2, the authors obtained well-defined Au nanoframes (Fig. 2d). The ridge thickness of the Au nanoframes could be controlled down to ~2 nm by adjusting the amount of Au precursor added. In principle, this approach can be readily extended to other types of Ag nanocrystals with twin boundaries and {111} facets on the surface, including icosahedra and penta-twinned rods, to obtain Au nanoframes without losing the structural features of the original templates. Using a related approach, Xue and co-workers have successfully synthesized sub-2 nm triangular Au nanoframes through selected deposition of Au onto the edges of Ag triangular nanoplates, followed by etching with H_2O_2 and NH_4OH [54]. Most recently, Qin and co-workers used a similar method to fabricate Ag-Pd bimetallic nanoframes by selectively co-depositing Pd and Ag atoms on the vertices and edges of Ag nanocubes, followed by selective etching of the original Ag templates in aqueous H_2O_2 [55,56]. The same group has also prepared bimetallic Ag-Au cubic nanoframes through a combination of co-reduction and H_2O_2 etching [57]. Furthermore, Huang and co-workers reported the synthesis of trimetallic Au-Ag-Pt nanorings through selective deposition of Pt on the {100} facets of Au-Ag alloyed decahedra, followed by etching with O_2 [58]. Finally, Gong, Nie and their co-workers have prepared Pt nanorings from Saturn-like Au-Pt core-shell nanoparticles by utilizing $CuCl_2$ in a simultaneous alloying-etching strategy [59].

Park and co-workers further applied this synthetic approach to the preparation of Au nanoframes containing an embedded Pt skeleton [60]. In this case, Pt atoms were selectively deposited on the vertices and edges of Au nanodisks. The Au templates were then selectively etched away through the addition of Au^{3+}, thus generating Au^{+} ions in the reaction solution and leading to the formation of Pt nanorings. Finally, the Au^{+} ions in the reaction solution were reduced and deposited onto the Pt nanoframe, resulting in the formation of an Au nanoring surrounding a Pt skeleton. Similarly, Au octahedral, cubic and rod-shaped nanoframes with a Pt skeleton could also be prepared using this protocol [61,62]. Unlike the Au nanoframes derived from Ag templates, all the nanostructures of this new type showed greater stability when exposed to harsh physiochemical environments such as O_2 plasma treatments and pH extremes, which can be ascribed to the structural integrity provided by the inner Pt skeleton and the absence of Ag atoms alloyed with the nanoframe.

In addition to the wet chemical routes, site-selected deposition can also be achieved through electrochemical means. As reported by Torimoto and co-workers, Au could be electrodeposited onto the vertices and edges of Ag nanocubes modified with 1-octanethiol [63]. The site-selected deposition of Au could be ascribed to the inhomogeneous distribution of defect sites formed in the self-assembled monolayer of 1-octanethiol on the surface of the Ag nanocubes. Due to the absence of 1-octanethiol at the vertices and edges of the Ag nanocubes, the newly formed Au atoms were preferentially deposited at these sites. After chemical etching with a mixture of H_2O_2 and H_2SO_4, Au cubic nanoframes were obtained.

As can be surmised from the above examples, a combination of site-selected deposition of one metal on a template made of another metal and subsequent removal of the template through etching is a simple and effective route to fabricate nanoframes. The exact morphology of the nanoframe structure could be

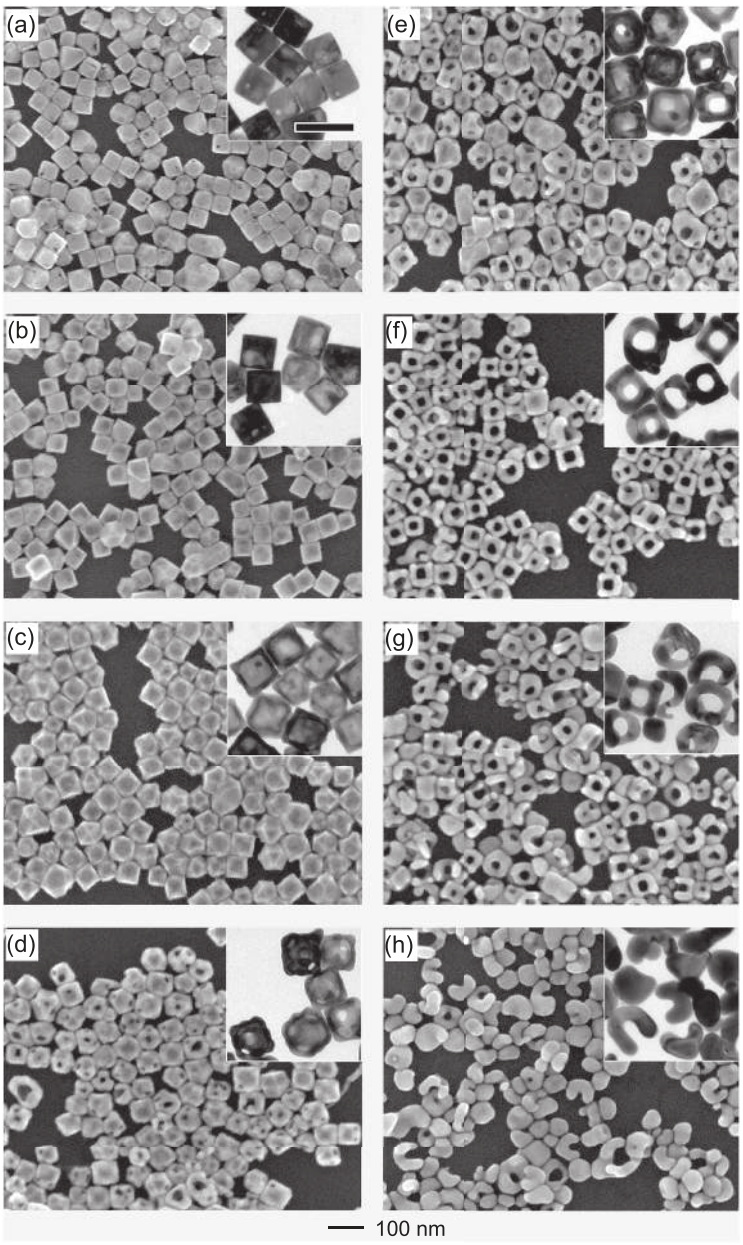

Figure 3. SEM and TEM (insets) images showing different stages of a galvanic replacement reaction involving the titration of Ag nanocubes with different volumes of 0.2 mM $AuCl_2^-$ in 1 mL increment ranging from (a) 1 mL to (h) 8 mL. The scale bar below the images applies to all SEM images. The scale bar in the insets represents 100 nm. Adapted with permission from [33].

varied by simply employing templates with different shapes, morphologies and surface configurations.

Dealloying of hollow or solid nanocrystals

Dealloying has been widely used for the fabrication of metal nanoframes. This process can start with either hollow or solid nanocrystals as the templates by following two distinct pathways: galvanic replacement and oxidative etching (Fig. 1b).

Galvanic replacement has been extensively explored as a means of dealloying. This process is driven by the difference in reduction potential between the two metals, with one serving as the cathode and the other as the anode [64]. For example, the reduction potential of Zn^{2+}/Zn^0 (–0.76 V *vs.* SHE) is lower than that of Cu^{2+}/Cu^0 (0.34 V *vs.* SHE). Consequently, when a Zn strip is immersed in a solution containing Cu^{2+}, Zn will be oxidized to Zn^{2+} whereas Cu^{2+} will be reduced to Cu [23]. Similarly to the etching process discussed above, the rate of galvanic replacement is driven primarily by the degree of difference in reduction potential between the metals involved, the concentration of the involved species and the reaction temperature.

Bimetallic nanoframes can be synthesized through a galvanic reaction between a template and a metal salt precursor possessing a higher reduction potential (e.g., Au, Pt and Pd) [33,65–79]. Ag is often used as the template material due to its lower reduction potential (Ag^+/Ag^0 0.8 V *vs.* SHE) when compared to many other noble metals and the large number of different shapes that has been reported for this relatively inexpensive noble metal. In an early report, our group described the synthesis of Au cubic nanoframes via the galvanic replacement reaction between Ag nanocubes and $AuCl_2^-$ [33]. In this example, one Ag atom is oxidized per Au atom being reduced [72]:

$$Ag(s) + AuCl_2^-(aq) \rightarrow AgCl(s) + Au(s) + Cl^-(aq). \quad (3)$$

Figure 3 shows SEM and TEM images of the products obtained at different stages of the galvanic replacement reaction where Ag nanocubes were titrated with different volumes of $AuCl_2^-$. In the initial stage, $AuCl_2^-$ was reduced through a redox reaction with surface Ag and the newly formed Au atoms were deposited onto the template surface. After this reaction had proceeded for a short period of time, enough Ag was removed from the template to form a pinhole on one of the six side faces (Fig. 3a). This pinhole served as a channel for mass transport, allowing for the shuttling of the $AuCl_2^-$ and the dissolved Ag^+ ions in and out of the template. As the reaction continued, the Au-enriched surface restructured due to atomic diffusion, closing the pinhole and generating a partially hollow nanoparticle (Fig. 3b). The interior of the nanoparticle continued to hollow out due to the diffusion of Ag to the surface, eventually forming a seamless Au-Ag alloyed nanobox with slightly truncated corners (Fig. 3c). With further

addition of $AuCl_2^-$, the Ag alloyed into the walls of the nanobox would be removed, resulting in the formation of multiple pores at the vertices and side faces of the nanostructure (Fig. 3d). These pores then coalesced due to Ag dealloying and surface restructuring, yielding cubic Au nanoframes (Fig. 3f). Past this point, the removal of the alloyed Ag compromised the structural integrity of the frame, resulting in its collapse into Au fragments without a specific morphology (Fig. 3g and h). It should be noted that, if $AuCl_2^-$ was replaced with $AuCl_4^-$, nanoframes could not be formed through this process. This is because the reduction of each Au^{3+} ion requires the oxidation of three Ag^+ ions. As a result, the dealloying of Ag from the template is too rapid, thereby depositing insufficient Au on the surface to produce a stable nanoframe.

As a variation of this approach, Li and co-workers recently demonstrated the synthesis of Au-Ag octahedral nanoframes through a modified one-pot galvanic replacement reaction [66]. Initially, truncated polyhedra of Ag were produced by reducing $AgNO_3$ with CuCl and octadecylamine. The galvanic replacement reaction was then initiated with the introduction of a $HAuCl_4$ solution. Similarly to the example of Au cubic nanoframes, Ag atoms were oxidized and dissolved, followed by the reduction and deposition of Au atoms. Due to the galvanic replacement between Ag and $AuCl_4^-$, octahedral hollow structures with pinholes on the {111} facets appeared after a reaction time of only 40 s. When the reaction time was increased to 20 min, all of the eight {111} facets of octahedra disappeared, resulting in the formation of octahedral Au-Ag bimetallic nanoframes with a ridge thickness less than 10 nm. A similar approach was used by Zitoun and co-workers to fabricate trimetallic Pt-Ni-Au octahedral nanoframes [80].

Most recently, Pt-Cu, Ir-Cu and Rh-Cu nanoframes have also been synthesized through dealloying based on galvanic replacement [81–86]. Huang and co-workers reported the one-pot preparation of Pt-Cu alloyed rhombic dodecahedral nanoframes by employing a precursor mixture of platinum(II) acetylacetonate and copper(II) chloride [81]. The Cu^{2+} precursor was rapidly reduced, thereby forming pure Cu nanocrystals. This was followed by the galvanic replacement between Cu and Pt^{2+}. The asynchronous reduction of the two metal salts occurred due to the relative difficulty in reducing platinum(II) acetylacetonate as compared to copper(II) chloride. The Cu content in the nanocrystals gradually decreased as the reaction proceeded. After 3 h, Pt-Cu nanoframes with a Pt:Cu ratio of 1:3 were obtained. Using a similar one-pot approach, Li and co-workers also demonstrated the synthesis of Ir-Cu nanoframes. The formation of Ir-Cu nanoframes involved the initial nucleation and growth of Cu nanostructures from copper(II) acetylacetonate, followed by galvanic replacement between Cu and Ir^{3+} from $IrCl_3$ at 170°C [84]. When using the as-prepared Ir-Cu nanoframes as templates, these authors further demonstrated the fabrication of Ir-Cu-Au trimetallic nanoframes through the addition of $HAuCl_4$ [84].

Another pathway for dealloying lies in oxidative etching [26,87–94]. This process is similar in nature to the chemical etching described in the previous section. However, rather than preparing a core-frame template and etching away the core, this approach utilizes an alloyed nanocrystal as the template. Etching is used to selectively remove one or more components from the template, inducing diffusion-based internal restructuring and producing nanoframes. In an early study, our group demonstrated the synthesis of Au cubic nanoframes by dealloying Au-Ag alloyed nanoboxes with an aqueous etchant [87]. We used Ag nanocubes of 50 nm in size as the templates (Fig. 4a). In the first step, Au-Ag alloy nanoboxes (Fig. 4b) were obtained based on the galvanic replacement reaction between Ag and $AuCl_4^-$:

$$3Ag(s) + AuCl_4^-(aq) \rightarrow 3Ag^+(aq) + Au(s) + 4Cl^-(aq). \quad (4)$$

By introducing an aqueous solution of $Fe(NO_3)_3$, Ag atoms could be selectively removed from the alloyed nanoboxes [95]. Increasing the amount of added $Fe(NO_3)_3$ resulted in the formation of Au-based nanocages (Fig. 4c) and finally cubic nanoframes (Fig. 4d). In addition to $Fe(NO_3)_3$, aqueous NH_4OH could also be used as an etchant to oxidize and dissolve Ag atoms, as facilitated by the formation of a $[Ag(NH_3)_2]^+$ complex in the presence of oxygen [96]. However, due to the weak etching power of NH_4OH, the Au-Ag alloyed nanoboxes etched in this manner produced a mixture of nanocages and nanoframes [87].

A combination of O_2 and a proper coordination ligand for the metal ions can also serve as a powerful etchant [1,97]. To this end, Yang, Stamenkovic and their co-workers reported the synthesis of Pt_3Ni nanoframes with a Pt-skin structure through the use of an O_2-based etchant [26]. First, $PtNi_3$ rhombic dodecahedra nanocrystals were synthesized in oleylamine (Fig. 4e). These nanocrystals possessed an inhomogeneous elemental distribution, with Pt and Ni concentrated at the edges and side faces, respectively. This phenomenon likely arose from a

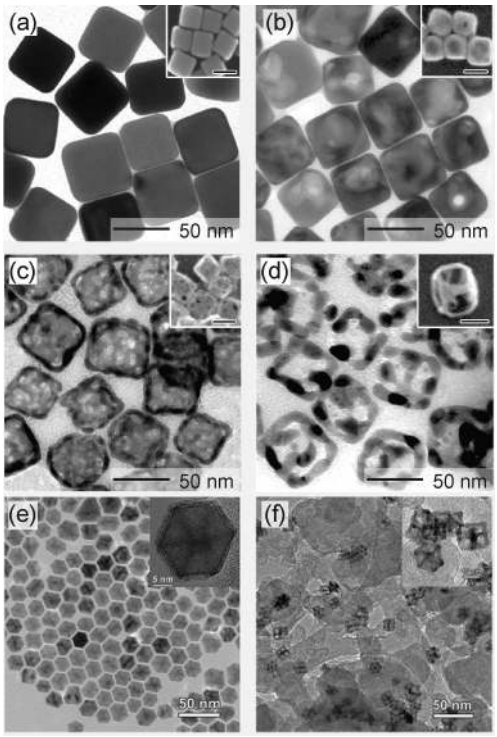

Figure 4. TEM and SEM (insets) images of (a) 50-nm Ag nanocubes, (b) Au/Ag nanoboxes prepared by galvanic replacement and (c) nanocages, and (d) nanoframes prepared with $Fe(NO_3)_3$ as an etchant for Ag. TEM images of (e) initial solid $PtNi_3$ polyhedra and (f) annealed Pt_3Ni nanoframes with Pt(111) skin on the surface (dispersed on high-surface area carbon). Adapted with permissions from [26,87].

combination of factors, including the rapid dissolution of Ni from the high-energy edges due to oxidative etching and galvanic replacement, the selective capping and stabilization of the Pt atoms at the surface by oleylamine, and the strain induced segregation of larger Pt atoms from smaller Ni [89]. The $PtNi_3$ nanocrystals were then suspended in hexane and heated at 120°C under the ambient conditions. During this process, the surface Ni atoms oxidized more readily than the Pt atoms in the presence of O_2, due to the higher reduction potential of Pt (Pt^{2+}/Pt^0 1.2 V *vs.* SHE) relative to Ni (Ni^{2+}/Ni^0 −0.25 V *vs.* SHE) [98]. The resultant Ni^{2+} and oleylamine can form a soluble metal complex, thereby extracting Ni^{2+} from the reaction and further driving the dissolution of Ni [99]. As dealloying continued, the composition of the nanocrystals changed from Ni-rich to Pt-rich, and ultimately stabilized in the form of Pt_3Ni [100]. Due to an inhomogeneous elemental distribution in the $PtNi_3$ rhombic dodecahedra, the Ni-rich interior of the polyhedral faces was more susceptible to dissolution, leaving behind Pt-rich edges [101]. Therefore, the initially solid $PtNi_3$ rhombic dodecahedra were gradually transformed into Pt_3Ni nanoframes. The nanoframes were subsequently dispersed on a carbon support and heated to between 370°C and 400°C under Ar, promoting atomic intra-diffusion to generate Pt_3Ni nanoframes with a Pt-skin on the surface (Fig. 4f). A similar method was also explored by other groups to produce Pt-Ni and Pt-Co nanoframes with various morphologies [90–93]. It should be noted that the Kirkendall effect is also, at times, invoked to explain the formation of the nanoframes. However, one must keep in mind that the Kirkendall effect is purely an intra-diffusion phenomenon and would not result in the removal of an elemental component from a nanoparticle.

Recently, Yan and co-workers synthesized Rh-Cu octahedral frames by using O_2 and HCl as the etchant [94]. The authors first prepared monodisperse Rh-Cu octahedra. Following this, the octahedra were loaded on carbon and cleaned by acetic acid. Most of the Cu atoms on the nanoparticle surface were removed during this process. Then, the octahedra were etched with O_2 and HCl, resulting in the formation of Rh-Cu octahedral nanoframes. This can be ascribed to the fact that Cu atoms are easier to be oxidized than Rh atoms due to the lower reduction potential of Cu (Cu^{2+}/Cu^0 0.34 V *vs.* reversible hydrogen electrode, RHE) in comparison with Rh (Rh^{3+}/Rh^0 0.76 V *vs.* RHE), and the tendency of Rh atoms to segregate at edges and surface layers of the nanostructure. Moreover, Rh-Pd-Cu trimetallic, nanopolyhedral frames have also been prepared using this method [94]. Hattori and co-workers utilized a similar approach to create Rh frame nanorods by etching Au-Rh core-shell nanorods with HCl [102].

Taken together, the successful fabrication of nanoframes through the dealloying process relies on our ability to control the galvanic replacement between different metals and to select a suitable etchant for use in oxidative etching.

APPLICATIONS

Photonic applications

The optical properties of noble-metal nanoframes have attracted attention in recent years due to their highly tunable and controllable plasmonic features [33–38,60,76,79]. For nanoframes made of Au and/or Ag, their LSPR properties are determined by a number of parameters, including edge length, ridge thickness, corner sharpness, elemental composition and dielectric environment [33,34]. Figure 5a shows the scattering spectra of different nanoframes calculated using the discrete dipole approximation (DDA) method. The nanoframes in question had a

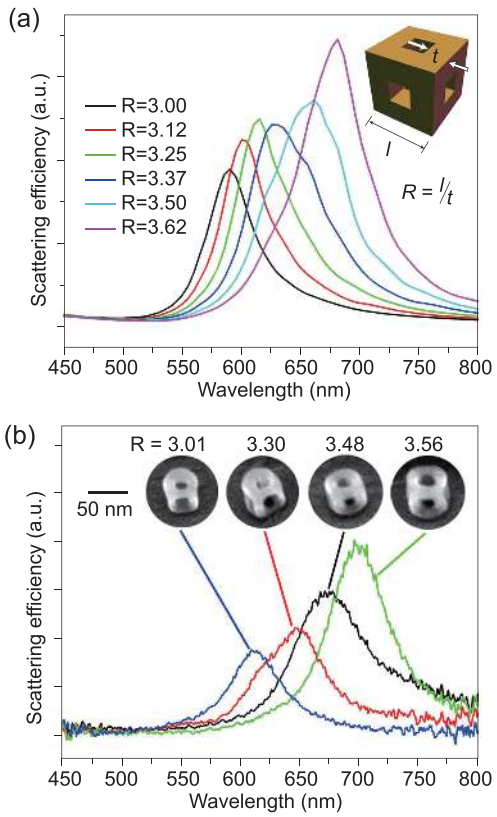

Figure 5. (a) DDA-calculated scattering spectra for nanoframes with an edge length of 57.0, 59.4, 61.8, 64.1, 66.5 and 68.9 nm, having a constant ridge thickness of 19 nm, together with a fixed composition of 89% Au and 11% Ag. The inset shows a schematic of the nanoframe used in these calculations, which has both sharp corners and edges. The red-shifts of the plasmon resonance peak increase with increasing ratio (R) between the outer edge length (l) and the ridge thickness (t). (b) Scattering spectra of individual Au cubic nanoframes and the SEM images of the corresponding nanoframes. Adapted with permission from [33].

constant ridge thickness of 19 nm and a fixed composition of 89% Au and 11% Ag, whereas the outer edge length was varied. The peak position red-shifted with the increase in the ratio (R) between the outer edge length (l) and the ridge thickness (t). This trend can be attributed to the increase in charge separation and the weakening of the restoring force for electron oscillation as the R-value increased, and it is essentially identical to what has been observed for the longitudinal mode of Au or Ag nanorods [33]. The computational results were further validated by experimental measurement of individual nanoframes. The resonance peak position was red-shifted with an increase in the R-value (Fig. 5b). Taken together, it is clear that the LSPR peak of nanoframes could be readily tuned by controlling the edge length and/or ridge thickness.

Due to the tunable LSPR, noble-metal nanoframes have the potential to be used for a number of photonic applications, such as optical sensing, surface-enhanced Raman scattering (SERS) and the destruction of cancer cells via the photothermal effect [34–38,79]. Owing to the coupling between the surface plasmons of the outer and inner surfaces, nanoframes have been found to exhibit stronger surface plasmonic fields and thus enhanced sensitivity in comparison with other types of Au nanostructures. For instance, El-Sayed and co-workers found that the sensitivity factor of Au nanoframes was 12, 7 and 3 times greater than that of Au nanospheres, nanocubes and nanorods, respectively. In general, the small-sized nanoframes with a larger R-value exhibited a larger sensitivity factor and thus excellent potential as nanosensors in the near-infrared region [34]. Interestingly, polycrystalline Au nanoframes have also been demonstrated with promising SERS activities. Gao and co-workers produced 23-nm Au nanoframes by using 7-nm AgI nanocubes as sacrificial templates [37]. The lattice mismatch between the AgI and Au resulted in the non-epitaxial overgrowth of Au on the template's vertices and edges. After the templates had been removed with methylamine, the remaining polycrystalline Au nanoframes displayed SERS signal that was 6 times stronger than Au spheres of a similar size.

Catalytic applications

Catalytic reactions primarily take place on the surface of heterogeneous catalysts. As a direct consequence of this, the atoms in the interior of the catalyst nanoparticles are excluded from participating in the reaction. The fabrication of nanoframes is an effective strategy for improving the utilization efficiency of atoms, and thus decreasing the loading and materials cost of a noble-metal catalyst. Due to the open 3D structure of nanoframes, both atoms on the outer and inner surfaces can take part in catalysis, resulting in increased activity. The various noble-metal nanoframes and their related catalytic applications are summarized in Table 1.

Yang, Stamenkovic and their co-workers found that the Pt_3Ni nanoframes synthesized with Pt-skin on the surface exhibited significantly enhanced activities toward the oxygen reduction reaction (ORR) relative to Pt-Ni and commercial state-of-the-art Pt/C electrocatalysts [26]. As shown in Fig. 6a, the specific activity of Pt_3Ni nanoframes at 0.95 V (*vs.* RHE) showed a 16-fold improvement *vs.* commercial Pt/C. The enhancement of specific activity could be attributed to the high specific

Table 1. The reported catalytic applications of noble-metal nanoframes with various shapes and compositions.

Catalytic reaction	The shape and composition of nanoframe
Oxygen reduction reaction	Polyhedral Pt_3Ni [26]; Cubic Pt [50]; Decahedral Pt-Cu [85]; Rhombic dodecahedral Cu_3Pt [104]
Hydrogen evolution reaction	Polyhedral Pt_3Ni modified with $Ni(OH)_2$ [26]
Electro-oxidation of methanol	Rhombic dodecahedral Pt-Cu [81,83]; Decahedral Pt-Cu [85]; Truncated octahedral Pt_3Ni decorated with Au islands [90]
Electro-oxidation of formic acid	Octahedral Pt-Cu [82]
Oxygen evolution reaction	Polyhedral Ir-Cu [84]; Truncated octahedral Rh-Cu [86]
Oxidation of *o*-phenylenediamine to 2,3-diaminophenazine	Cubic Pd-Rh [51]
Hydrazine decomposition	Octahedral Rh-Cu [94]
CO oxidation	Hexagonal Pt [105]

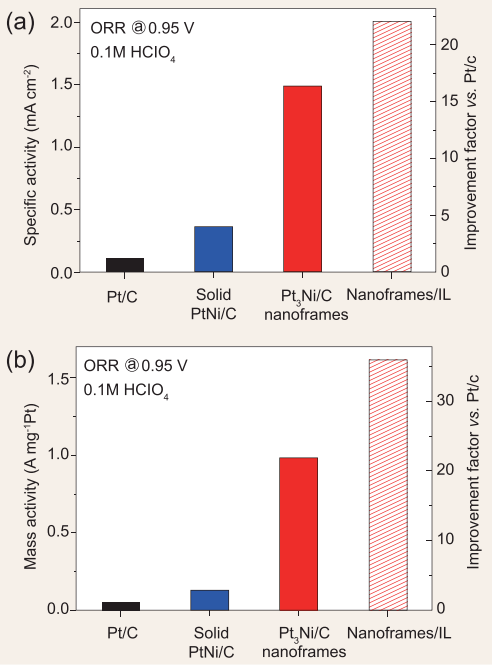

Figure 6. (a) Specific activities and (b) mass activities of commercial Pt/C, solid Pt-Ni/C, Pt_3Ni/C nanoframes and ionic liquid-encapsulated Pt_3Ni nanoframes/C measured at 0.95 V, and improvement factors *vs.* Pt/C catalysts. Adapted with permission from [26].

surface area derived from the open structure of a Pt_3Ni nanoframe, as well as the two monolayers of surface-strained Pt-skin. This strain altered the electronic properties of the top-most Pt atoms by changing their interatomic distances, thereby lowering the binding energy of oxygen-containing poison species and leading to a higher number of available catalytic sites. *In situ* X-ray absorption spectroscopy revealed that surface composition was crucial to the ORR activity of the nanoframe catalyst [103]. The impact of both the high specific activity and the open architecture resulted in a 22-fold enhancement in mass activity *vs.* the Pt/C catalyst (Fig. 6b). Moreover, when the Pt_3Ni nanoframes were modified with $Ni(OH)_2$ clusters through electrochemical deposition, the obtained catalyst exhibited an enhancement in activity of nearly one order of magnitude relative to the Pt/C for the hydrogen evolution reaction (HER). Furthermore, trimetallic Pt_3Ni polyhedral nanoframes decorated with Au islands displayed higher activity and stability during electro-oxidation of methanol when compared to their undecorated solid and frame counterparts, respectively [90].

Additionally, Wang and co-workers demonstrated that their Pt-Cu octahedral nanoframes exhibited significantly enhanced specific activity toward the electro-oxidation of formic acid when compared with the commercial Pt black and Pt/C catalysts [82]. The improvement in activity can be attributed to the nanoframe structure and the possible synergetic effect between Pt and Cu components. For the electro-oxidation of methanol, Pt-Cu nanocatalysts with a frame structure also displayed higher specific and mass activities than the commercial Pt black and Pt/C catalysts [81,83,85]. The alloyed Cu_3Pt nanoframes with rhombic dodecahedral morphology were shown to be more effective for ORR in comparison with the Cu-Pt core-shell rhombic dodecahedra [104]. Moreover, due to the highly open structure, Ir-Cu nanoframes exhibited significantly enhanced activity toward oxygen evolution reaction (OER) in alkaline media, as compared to solid Ir-Cu nanoparticles [84]. Similarly, Rh-Cu truncated octahedral nanoframes were shown to be an effective catalyst for driving OER, compared to both Cu-Rh core-shells and Rh-Cu twinned nanorod frames [86].

In addition to electrochemical reactions, nanoframe-based catalysts have also demonstrated their structural advantage in other catalytic systems

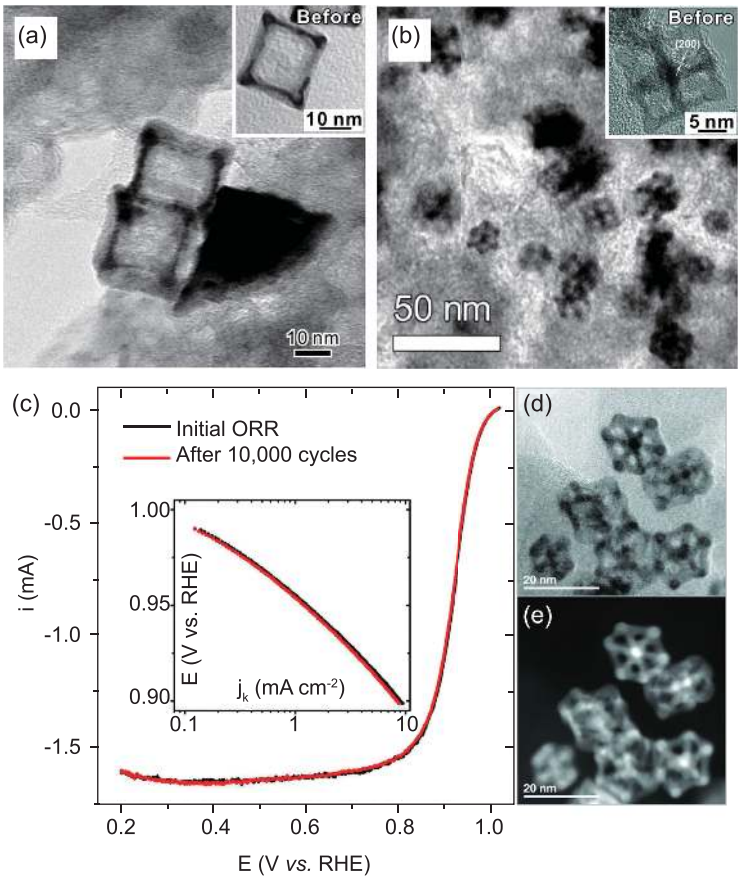

Figure 7. (a) TEM images of Rh cubic nanoframes/C before (inset) and after being heated in air at 500°C for 1 h. (b) TEM images of Pt_3Ni nanoframes/C catalysts before (inset) and after being annealed at 400°C in Ar. (c) ORR polarization curves and corresponding Tafel plots (inset) of Pt_3Ni frames before and after 10 000 potential cycles between 0.6 and 1.0 V. (d and e) Bright-field STEM (d) and dark-field STEM images (e) of Pt_3Ni nanoframes/C after 10 000 cycles. Adapted with permissions from [26,46].

[51,94,105]. For instance, in the oxidation of *o*-phenylenediamine to 2,3-diaminophenazine, Yang and co-workers reported that Pd-Rh nanoframes showed enhanced conversion efficiency relative to Pd-Rh core-frame nanostructures [51]. When compared with Rh-Cu octahedra, Rh-Cu octahedral frames showed higher catalytic activity toward hydrazine decomposition, owing to the presence of more accessible active sites on the surface [94].

The particular configuration of the nanoframe structure can also improve the thermal and chemical stabilities of a catalyst. As shown in Fig. 7a, the structure of Rh cubic nanoframes remained stable after heating at 500°C for 1 h [46]. Yang, Stamenkovic and their co-workers also reported that the Pt_3Ni nanoframe structure was preserved after annealing at 400°C for several hours under Ar (Fig. 7b) [26]. Moreover, the Pt_3Ni nanoframes exhibited remarkable durability during ORR. After 10 000 electrochemical cycles between 0.6 and 1.0 V (*vs.* RHE), the intrinsic activity of Pt_3Ni nanoframes was retained (Fig. 7c), which can be ascribed to the low dissolution rate of Pt. This, in turn, was a result of the particular electronic structure of the Pt-skin surface and the optimized Pt-skin thickness of at least two monolayers [106,107]. Moreover, both bright-field and dark-field scanning transmission electron microscopy (STEM) images (Fig. 7d and e) confirmed that the frame structure was retained after 10 000 cycles.

CONCLUSION AND OUTLOOK

In conclusion, noble-metal nanoframes can be synthesized through two different strategies based on site-selected deposition and etching, and dealloying of hollow and solid bimetallic (or multi-metallic) nanocrystals. The formation of nanoframes may involve mechanisms such as galvanic replacement, oxidative etching, intra-particle atomic diffusion or a combination of them. Noble-metal nanoframes are effective heterogeneous catalysts owing to their 3D, open structures, large specific surface areas and the presence of highly active sites. Additionally, nanoframes made of Au and/or Ag also exhibited unique and highly tunable optical properties such as LSPR.

Despite the remarkable progress in recent years, there are remaining avenues for further improvement. For example, achieving a precise control over facets is still a grand challenge, particularly as the ridges of nanoframes decreases to a level of only a few nanometers thick. Without a precise control over the facet, it is difficult to manage catalytic activity and selectivity. In addition, the thickness of the nanoframe ridges can be reduced further. Currently, the thinnest ridge thickness reported in literature for noble-metal nanoframes is around 2 nm. Shrinking the ridge thickness to a few atoms can further increase the utilization efficiency of atoms, thereby reducing the materials cost of the catalyst.

There are also concerns about the structural stability of the nanoframes. For example, a recent study, based on the density functional theory (DFT), of a Rh nanoframe with a simple cubic structure indicated that the edge length must be at least 2 nm in order to retain the frame structure. The models became convex or collapsed for ridge thickness of less than 0.5 nm and edge length of less than 2 nm, respectively [108]. Since all the reported nanoframes possess edge length on the tens of nanometers scale, further reduction in size may be possible without destabilizing the nanostructure.

Similar to the observed effects of facet control, engineering the crystal phase of a catalytic

nanoparticle may provide an additional knob to optimize the catalytic performance. Previous catalytic comparisons between nanoparticles composed of different crystal phases of the same metal have shown significant differences in activity [52,109–114]. Although such a comparison study is yet to be reported for nanoframe structures, it may be achievable by optimizing the synthetic parameters, including temperature, pressure and the selection of appropriate elemental precursors and templates.

Finally, it may be prudent to expand our synthetic methods for the preparation of noble-metal nanoframes beyond wet chemistry. Recent work has shown that nanoframes composed of Au, Pd and Pt could be prepared through a galvanic replacement process utilizing nanoparticle templates grown on a substrate using thin metal film dewetting [115]. This approach has the advantage of eschewing all capping agents, resulting in a cleaner nanocrystal surface, which is crucial for the effective use of nanoframes as catalysts. While these authors still used a precursor solution to initiate the galvanic replacement, previous work has demonstrated that an elastomer stamp infused with metal precursor could also be used to drive the replacement reaction under dry conditions [116].

FUNDING

This work was supported in part by start-up funds from the Georgia Institute of Technology and a grant from the NSF (CHE 1505441). As a visiting PhD student from Xiamen University, XW also received partial support from the China Scholarship Council. AR was supported by the NSF Graduate Research Fellowship Award.

REFERENCES

1. Xia Y, Xiong Y and Lim B *et al.* Shape-controlled synthesis of metal nanocrystals: simple chemistry meets complex physics? *Angew Chem Int Ed* 2009; **48**: 60—103.
2. Wu J and Yang H. Platinum-based oxygen reduction electrocatalysts. *Acc Chem Res* 2013; **46**: 1848—57.
3. Quan Z, Wang Y and Fang J. High-index faceted noble metal nanocrystals. *Acc Chem Res* 2013; **46**: 191—202.
4. Sun Y. Interfaced heterogeneous nanodimers. *Natl Sci Rev* 2015; **2**: 329—48.
5. Zhou K and Li Y. Catalysis based on nanocrystals with well-defined facets. *Angew Chem Int Ed* 2011; **51**: 602—13.
6. Guo S, Zhang S and Sun S. Tuning nanoparticle catalysis for the oxygen reduction reaction. *Angew Chem Int Ed* 2013; **52**: 8526—44.
7. Liu H-L, Nosheen F and Wang X. Noble metal alloy complex nanostructures: controllable synthesis and their electrochemical property. *Chem Soc Rev* 2015; **44**: 3056—78.
8. Zhang J, Yang H and Fang J *et al.* Synthesis and oxygen reduction activity of shape-controlled Pt_3Ni nanopolyhedra. *Nano Lett* 2010; **10**: 638—44.
9. Choi S-I, Xie S and Shao M *et al.* Synthesis and characterization of 9 nm Pt-Ni octahedra with a record high activity of 3.3 A/mg_{Pt} for the oxygen reduction reaction. *Nano Lett* 2013; **13**: 3420—5.
10. Strasser P, Koh S and Anniyev T *et al.* Lattice-strain control of the activity in dealloyed core-shell fuel cell catalysts. *Nat Chem* 2010; **2**: 454—60.
11. Sasaki K, Naohara H and Choi Y *et al.* Highly stable Pt monolayer on PdAu nanoparticle electrocatalysts for the oxygen reduction reaction. *Nat Commun* 2012; **3**: 1115.
12. Zhang J, Vukmirovic MB and Xu Y *et al.* Controlling the catalytic activity of platinum-monolayer electrocatalysts for oxygen reduction with different substrates. *Angew Chem Int Ed* 2005; **44**: 2132—5.
13. Xie S, Choi S-I and Lu N *et al.* Atomic layer-by-layer deposition of Pt on Pd nanocubes for catalysts with enhanced activity and durability toward oxygen reduction. *Nano Lett* 2014; **14**: 3570—6.
14. Park J, Zhang L and Choi S-I *et al.* Atomic layer-by-layer deposition of platinum on palladium octahedra for enhanced catalysts toward the oxygen reduction reaction. *ACS Nano* 2015; **9**: 2635—47.
15. Wang X, Choi S-I and Roling LT *et al.* Palladium–platinum core-shell icosahedra with substantially enhanced activity and durability towards oxygen reduction. *Nat Commun* 2015; **6**: 7594.
16. Mahmoud MA, Saira F and El-Sayed MA. Experimental evidence for the nanocage effect in catalysis with hollow nanoparticles. *Nano Lett* 2010; **10**: 3764—9.
17. Wang JX, Ma C and Choi Y *et al.* Kirkendall effect and lattice contraction in nanocatalysts: a new strategy to enhance sustainable activity. *J Am Chem Soc* 2011; **133**: 13551—7.
18. Zhang L, Roling LT and Wang X *et al.* Platinum-based nanocages with subnanometer-thick walls and well-defined, controllable facets. *Science* 2015; **349**: 412—6.
19. Wang X, Figueroa-Cosme L and Yang X *et al.* Pt-based icosahedral nanocages: using a combination of {111} facets, twin defects, and ultrathin walls to greatly enhance their activity toward oxygen reduction. *Nano Lett* 2016; **16**: 1467—71.
20. Huang X, Tang S and Zhang H *et al.* Controlled formation of concave tetrahedral/trigonal bipyramidal palladium nanocrystals. *J. Am. Chem. Soc.* 2009; **131**: 13916—7.
21. Jia Y, Jiang Y and Zhang J *et al.* Unique excavated rhombic dodecahedral $PtCu_3$ alloy nanocrystals constructed with ultrathin nanosheets of high-energy {110} facets. *J Am Chem Soc* 2014; **136**: 3748–51.
22. Chen Q, Yang Y and Cao Z *et al.* Excavated cubic platinum-tin alloy nanocrystals constructed from ultrathin nanosheets with enhanced electrocatalytic activity. *Angew Chem Int Ed* 2016; **55**: 9021–5.

23. Skrabalak SE, Chen J and Sun Y *et al.* Gold nanocages: synthesis, properties, and applications. *Acc Chem Res* 2008; **41**: 1587–95.
24. Sneed BT, Brodsky CN and Kuo C-H *et al.* Nanoscale-phase-separated Pd-Rh boxes synthesized via metal migration: an archetype for studying lattice strain and composition effects in electrocatalysis. *J Am Chem Soc* 2013; **135**: 14691–700.
25. Sun Y, Wiley BJ and Li Z-Y *et al.* Synthesis and optical properties of nanorattles and multiple-walled nanoshells/nanotubes made of metal alloys. *J Am Chem Soc* 2004; **126**: 9399–406.
26. Chen C, Kang Y and Huo Z *et al.* Highly crystalline multimetallic nanoframes with three-dimensional electrocatalytic surfaces. *Science* 2014; **342**: 1339–43.
27. Kim H, Khi NT and Yoon J *et al.* Fabrication of hierarchical Rh nanostructures by understanding the growth kinetics of facet-controlled Rh nanocrystals. *Chem Commun* 2013; **49**: 2225–7.
28. Park J, Oh A and Baik H *et al.* One pot synthesis of nanoscale phase-segregated PdPt nanoarchitectures via unusual Pt-doping induced structural reorganization of a Pd nanosheet into a PdPt nanotent. *Nanoscale* 2014; **6**: 10551–5.
29. Lee KW, Park J and Lee H *et al.* Morphological evolution of 2D Rh nanoplates to 3D Rh concave nanotents, hierarchically stacked nanoframes, and hierarchical dendrites. *Nanoscale* 2015; **7**: 3460–5.
30. Fang Z, Wang Y and Liu C *et al.* Rational design of metal nanoframes for catalysis and plasmonics. *Small* 2015; **11**: 2593–605.
31. Ni B and Wang X. Face the edges: catalytic active sites of nanomaterials. *Adv Sci* 2015; **2**: 10.1002/advs.201500085.
32. Chen J, Lim B and Lee EP *et al.* Shape-controlled synthesis of platinum nanocrystals for catalytic and electrocatalytic applications. *Nano Today* 2009; **4**: 81–95.
33. Au L, Chen Y and Zhou F *et al.* Synthesis and optical properties of cubic gold nanoframes. *Nano Res* 2008; **1**: 441–9.
34. Mahmoud MA and El-Sayed MA. Gold nanoframes: very high surface plasmon fields and excellent near-infrared sensors. *J Am Chem Soc* 2010; **132**: 12704–10.
35. Mahmoud MA, Snyder B and El-Sayed MA. Surface plasmon fields and coupling in the hollow gold nanoparticles and surface-enhanced Raman spectroscopy: theory and experiment. *J Phys Chem C* 2010; **114**: 7436–43.
36. Chew WS, Pedireddy S and Lee YH *et al.* Nanoporous gold nanoframes with minimalistic architectures: lower porosity generates stronger surface-enhanced Raman scattering capabilities. *Chem Mater* 2015; **27**: 7827–34.
37. Zhang L, Liu T and Liu K *et al.* Gold nanoframes by nonepitaxial growth of Au on AgI nanocrystals for surface-enhanced Raman spectroscopy. *Nano Lett* 2015; **15**: 4448–54.
38. Karampelas IH, Liu K and Alali F *et al.* Plasmonic nanoframes for photothermal energy conversion. *J Phys Chem C* 2016; **120**: 7256–64.
39. Zou S and Schatz GC. Silver nanoparticle array structures that produce giant enhancements in electromagnetic fields. *Chem Phys Lett* 2005; **403**: 62–7.
40. Oldenburg SJ, Averitt RD and Westcott SL *et al.* Nanoengineering of optical resonances. *Chem Phys Lett* 1998; **288**: 243–247.
41. Jain PK, Huang X and El-Sayed IH *et al.* Noble metals on the nanoscale: optical and photothermal properties and some applications in imaging, sensing, biology, and medicine. *Acc Chem Res* 2008; **41**: 1578–86.
42. Kelly KL, Coronado E and Zhao LL *et al.* The optical properties of metal nanoparticles: the influence of size, shape, and dielectric environment. *J Phys Chem B* 2003; **107**: 668–77.
43. Sherry LJ, Jin R and Mirkin CA *et al.* Localized surface plasmon resonance spectroscopy of single silver triangular nanoprisms. *Nano Lett* 2006; **6**: 2060–5.
44. Yu Y-Y, Chang S-S and Lee C-L *et al.* Gold nanorods: electrochemical synthesis and optical properties. *J Phys Chem B* 1997; **101**: 6661–4.
45. Xia X, Xie S and Liu M *et al.* On the role of surface diffusion in determining the shape or morphology of noble-metal nanocrystals. *Proc Natl Acad Sci U S A* 2013; **110**: 6669–73.
46. Xie S, Lu N and Xie Z *et al.* Synthesis of Pd-Rh core-frame concave nanocubes and their conversion to Rh cubic nanoframes by selective etching of the Pd cores. *Angew Chem Int Ed* 2012; **51**: 10266–70.
47. Lim B, Jiang MJ and Tao J *et al.* Shape-controlled synthesis of Pd nanocrystals in aqueous solutions. *Adv Funct Mater* 2009; **19**: 189–200.
48. Sau TK and Rogach AL. *Complex-shaped metal nanoparticles*. Weinheim: Wiley-VCH, 2012.
49. Xie S, Peng H-C and Lu N *et al.* Confining the nucleation and overgrowth of Rh to the {111} facets of Pd nanocrystal seeds: the roles of capping agent and surface diffusion. *J Am Chem Soc* 2013; **135**: 16658–67.
50. Park J, Wang H and Vara M *et al.* Platinum cubic nanoframes with enhanced catalytic activity and durability toward oxygen reduction. *ChemSusChem* 2016; **9**: 2855–61.
51. Ye W, Kou S and Guo X *et al.* Controlled synthesis of bimetallic Pd-Rh nanoframes and nanoboxes with high catalytic performances. *Nanoscale* 2015; **7**: 9558–62.
52. Ye H, Wang Q and Catalano M *et al.* Ru nanoframes with an fcc structure and enhanced catalytic properties. *Nano Lett* 2016; **16**: 2812–7.
53. McEachran M, Keogh D and Pietrobon B *et al.* Ultrathin gold nanoframes through surfactant-free templating of faceted pentagonal silver nanoparticle. *J Am Chem Soc* 2011; **133**: 8066–9.
54. Shahjamali MM, Bosman M and Cao S *et al.* Surfactant-free sub-2 nm ultrathin triangular gold nanoframes. *Small* 2013; **9**: 2880–6.
55. Li J, Liu J and Yang Y *et al.* Bifunctional Ag@Pd-Ag nanocubes for highly sensitive monitoring of catalytic reactions by surface-enhanced Raman spectroscopy. *J Am Chem Soc* 2015; **137**: 7039–42.
56. Li J, Sun X and Qin D. Ag-enriched Ag-Pd bimetallic nanoframes and their catalytic properties. *ChemNanoMat* 2016; **2**: 494–9.
57. Sun X and Qin D. Co-titration of $AgNO_3$ and $HAuCl_4$: a new route to the synthesis of Ag@Ag-Au core-frame nanocubes with enhanced plasmonic and catalytic properties. *J Mater Chem C* 2015; **3**: 11833–41.
58. Han S, Zhou G and Fu Y *et al.* The alloying effect and AgCl-directing growth for synthesizing a trimetallic nanoring with improved SERS. *Nanoscale* 2015; **7**: 20414–25.
59. Huang Z, Raciti D and Yu S *et al.* Synthesis of platinum nanotubes and nanorings via simultaneous metal alloying and etching. *J Am Chem Soc* 2016; **138**: 6332–5.
60. Jang H-J, Ham S and Acapulco JAI *et al.* Fabrication of 2D Au nanorings with Pt framework. *J Am Chem Soc* 2014; **136**: 17674–80.
61. Ham S, Jang H-J and Song Y *et al.* Octahedral and cubic gold nanoframes with platinum framework. *Angew Chem Int Ed* 2015; **54**: 9025–8.
62. Lee S, Jang H-J and Jang HY *et al.* Synthesis and optical property characterization of elongated AuPt and Pt@Au metal nanoframes. *Nanoscale* 2016; **8**: 4491–4.
63. Okazaki K, Yasui J and Torimoto T. Electrochemical deposition of gold frame structure on silver nanocubes. *Chem Commun* 2009; 2917–9.
64. Cobley CM and Xia Y. Engineering the properties of metal nanostructures via galvanic replacement reactions. *Mater Sci Eng R* 2010; **70**: 44–62.

65. Métraux GS, Cao YC and Jin R *et al.* Triangular nanoframes made of gold and silver. *Nano Lett* 2003; **3**: 519—22.
66. Hong X, Wang D and Cai S *et al.* Single-crystalline octahedral Au-Ag nanoframes. *J Am Chem Soc* 2012; **134**: 18165—8.
67. Si G, Ma Z and Li K *et al.* Triangular Au-Ag nanoframes with tunable surface plasmon resonance signal from visible to near-infrared region. *Plasmonics* 2011; **6**: 241—4.
68. Wan D, Xia X and Wang Y *et al.* Robust synthesis of gold cubic nanoframes through a combination of galvanic replacement, gold deposition, and silver dealloying. *Small* 2013; **9**: 3111—7.
69. Tsuji M, Kidera T and Yajima A *et al.* Synthesis of Ag-Au and Ag-Pd alloy triangular hollow nanoframes by galvanic replacement reactions without and with post-treatment using NaCl in an aqueous solution. *CrystEngComm* 2014; **16**: 2684—91.
70. Tsuji M, Hamasaki M and Yajima A *et al.* Synthesis of Pt-Ag alloy triangular nanoframes by galvanic replacement reactions followed by saturated NaCl treatment in an aqueous solution. *Mater Lett* 2014; **121**: 113—7.
71. Polavarapu L and Liz-Marzán LM. Growth and galvanic replacement of silver nanocubes in organic media. *Nanoscale* 2013; **5**: 4355—61.
72. Au L, Lu X and Xia Y. A comparative study of galvanic replacement reactions involving Ag nanocubes and $AuCl_2^-$ or $AuCl_4^-$. *Adv Mater* 2008; **20**: 2517—22.
73. Aherne D, Gara M and Kelly JM *et al.* From Ag nanoprisms to triangular AuAg nanoboxes. *Adv Funct Mater* 2010; **20**: 1329—38.
74. Sun J, Wang X and Liu J *et al.* Highly stable Ag-Au nanoplates and nanoframes for two-photon luminescence. *RSC Adv* 2014; **4**: 35263—7.
75. Kim MH, Lee J-J and Im SH *et al.* Synthesis of hex nut shaped Au-Ag nanostructures via a galvanic replacement reaction and their optical properties. *CrystEngComm* 2013; **15**: 6335—9.
76. Bai T, Tan Y and Zou J *et al.* $AuBr_2^-$-engaged galvanic replacement for citrate-capped Au-Ag alloy nanostructures and their solution-based surface-enhanced Raman scattering activity. *J Phys Chem C* 2015; **119**: 28597—604.
77. Sun Y and Xia Y. Triangular nanoplates of silver: synthesis, characterization, and use as sacrificial templates for generating triangular nanorings of gold. *Adv Mater* 2003; **15**: 695–9.
78. Personick ML, Langille MR and Wu J *et al.* Synthesis of gold hexagonal bipyramids directed by planar-twinned silver triangular nanoprisms. *J Am Chem Soc* 2013; **135**: 3800–3.
79. Parthiban MSP and Balakumar S. Synthesis of silver and silver/gold anisotropic nanostructures for surface enhanced Raman spectroscopy applications. *J Nanosci Nanotechnol* 2013; **13**: 8190–8.
80. Shviro M, Polani S and Zitoun D. Hollow octahedral and cuboctahedral nanocrystals of ternary Pt-Ni-Au alloys. *Nanoscale* 2015; **7**: 13521—9.
81. Ding J, Zhu X and Bu L *et al.* Highly open rhombic dodecahedral PtCu nanoframes. *Chem Commun* 2015; **51**: 9722—5.
82. Nosheen F, Zhang Z-C and Zhuang J *et al.* One-pot fabrication of single-crystalline octahedral Pt-Cu nanoframes and their enhanced electrocatalytic activity. *Nanoscale* 2013; **5**: 3660—3.
83. Yu X, Li L and Su W *et al.* Platinum-copper nanoframes: one-pot synthesis and enhanced electrocatalytic activity. *Chem Eur J* 2016; **22**: 4960—5.
84. Pei J, Mao J and Liang X *et al.* Ir-Cu nanoframes: one-pot synthesis and efficient electrocatalysts for oxygen evolution reaction. *Chem Commun* 2016; **52**: 3793—6.
85. Zhang Z, Luo Z and Chen B *et al.* One-pot synthesis of highly anisotropic five-fold-twinned PtCu nanoframes used as a bifunctional electrocatalyst for oxygen reduction and methanol oxidation. *Adv Mater* 2016; **28**: 10.1002/adma.201603075.
86. Park J, Kim J and Yang Y *et al.* RhCu 3D nanoframe as a highly active electrocatalyst for oxygen evolution reaction under alkaline condition. *Adv Sci* 2016; **3**: 10.1002/advs.201500252.
87. Lu X, Au L and McLellan J *et al.* Fabrication of cubic nanocages and nanoframes by dealloying Au/Ag alloy nanoboxes with an aqueous etchant based on $Fe(NO_3)_3$ or NH_4OH. *Nano Lett* 2007; **7**: 1764—9.
88. Yoon D, Park S and Park J *et al.* One pot synthesis of hollow Cu-doped Ru octahedral nanocages via an in situ generated metastable Cu nanoparticle template. *Nanoscale* 2014; **6**: 12397—402.
89. Oh A, Baik H and Choi DS *et al.* Skeletal octahedral nanoframe with Cartesian coordinates via geometrically precise nanoscale phase segregation in a Pt@Ni core-shell nanocrystal. *ACS Nano* 2015; **9**: 2856—67.
90. Wu Y, Wang D and Zhou G *et al.* Sophisticated construction of Au islands on Pt-Ni and ideal trimetallic nanoframe catalyst. *J Am Chem Soc* 2014; **136**: 11594—7.
91. Wang Y, Chen Y and Nan C *et al.* Phase-transfer interface promoted corrosion from $PtNi_{10}$ nanoctahedra to Pt_4Ni. *Nano Res* 2015; **8**: 140—55.
92. Ding J, Bu L and Guo S *et al.* Morphology and phase controlled construction of Pt-Ni nanostructures for efficient electrocatalysis. *Nano Lett* 2016; **16**: 2762—7.
93. Becknell N, Zheng C and Chen C *et al.* Synthesis of $PtCo_3$ polyhedral nanoparticles and evolution to Pt_3Co nanoframes. *Surf Sci* 2016; **648**: 328—32.
94. Zhang Z-P, Zhu W and Yan C-H *et al.* Selective synthesis of rhodium-based nanoframe catalysts by chemical etching of 3d metals. *Chem Commun* 2015; **51**: 3997—4000.
95. Xia Y, Kim E and Whitesides GM. Microcontact printing of alkanethiols on silver and its application in microfabrication. *J Electrochem Soc* 1996; **143**: 1070—9.
96. Hunyadi SE and Murphy CJ. Bimetallic silver-gold nanowires: fabrication and use in surface-enhanced Raman scattering. *J Mater Chem* 2006; **16**: 3929—35.
97. Zheng Y, Zeng J and Ruditskiy A *et al.* Oxidative etching and its role in manipulating the nucleation and growth of noble-metal nanocrystals. *Chem Mater* 2014; **26**: 22—33.
98. Xia X, Wang Y and Ruditskiy A *et al.* 25th anniversary article: galvanic replacement: a simple and versatile route to hollow nanostructures with tunable and well-controlled properties. *Adv Mater* 2013; **25**: 6313—33.
99. Wang D and Li Y. Effective octadecylamine system for nanocrystal synthesis. *Inorg Chem* 2011; **50**: 5196—202.
100. Dahmani CE, Cadeville MC and Sanchez JM *et al.* Ni-Pt phase diagram: experiment and theory. *Phys Rev Lett* 1985; **55**: 1208—11.
101. Niu Z, Becknell N and Yu Y *et al.* Anisotropic phase segregation and migration of Pt in nanocrystals en route to nanoframe catalysts. *Nat Mater* 2016; **15**: 10.1038/NMAT4724.
102. Tsuji M, Nakashima Y and Yajima A *et al.* Formation of Rh frame nanorods using Au nanorods as sacrificial templates. *CrystEngComm* 2015; **17**: 6955—61.
103. Becknell N, Kang Y and Chen C. Atomic structure of Pt_3Ni nanoframe electrocatalysts by in situ X-ray absorption spectroscopy. *J Am Chem Soc* 2015; **137**: 15817—24.

104. Han L, Liu H and Cui P *et al.* Alloy Cu_3Pt nanoframes through the structure evolution in Cu-Pt nanoparticles with a core-shell construction. *Sci Rep* 2014; **4**: 6414.
105. Choi B-S, Kim SM and Gong J *et al.* One-pot self-templating synthesis of Pt hollow nanostructures and their catalytic properties for CO oxidation. *Chem Eur J* 2014; **20**: 11669—74.
106. Stamenkovic VR, Fowler B and Mun BS *et al.* Improved oxygen reduction activity on $Pt_3Ni(111)$ via increased surface site availability. *Science* 2007; **315**: 493—7.
107. Wang C, Chi M and Li D *et al.* Design and synthesis of bimetallic electrocatalyst with multilayered Pt-skin surfaces. *J Am Chem Soc* 2011; **133**: 14396—403.
108. Folsom B. Carbon pillars and metallic nanoframes: a density functional theory study. Master's thesis, Arizona State University, 2014.
109. Fan Z and Zhang H. Crystal phase-controlled synthesis, properties and applications of noble metal nanomaterials. *Chem Soc Rev* 2016; **45**: 63—82.
110. Huang X, Li S and Huang Y *et al.* Synthesis of hexagonal close-packed gold nanostructures. *Nat Commun* 2011; **2**: 292.
111. Fan Z, Bosman M and Huang X *et al.* Stabilization of 4H hexagonal phase in gold nanoribbons. *Nat Commun* 2015; **6**: 7684.
112. Fan Z, Huang X and Han Y *et al.* Surface modification-induced phase transformation of hexagonal close-packed gold square sheets. *Nat Commun* 2015; **6**: 6571.
113. Fan Z, Zhu Y and Huang X *et al.* Synthesis of ultrathin face-centered-cubic Au@Pt and Au@Pd core–shell nanoplates from hexagonal-close-packed Au square sheets. *Angew Chem Int Ed* 2015; **54**: 5672–6.
114. Fan Z, Luo Z and Huang X *et al.* Synthesis of 4H/fcc noble multimetallic nanoribbons for electrocatalytic hydrogen evolution reaction. *J Am Chem Soc* 2016; **138**: 1414–9.
115. Hajfathalian M, Gilroy KD and Golze SD *et al.* A Wulff in a cage: the confinement of substrate-based structures in plasmonic nanoshells, nanocages, and nanoframes using galvanic replacement. *ACS Nano* 2016; **10**: 6354—62.
116. Zhang Q, Lee YH and Phang IY *et al.* Bimetallic platonic Janus nanocrystals. *Langmuir* 2013; **29**: 12844—51.